International Journal of Mechanical Sciences xxx (xxxx) xxx



Contents lists available at ScienceDirect

International Journal of Mechanical Sciences

journal homepage: www.elsevier.com/locate/ijmecsci



Physics and chemistry-based phase-field constitutive framework for thermo-chemically aged elastomer

Aimane Najmeddine^a, Maryam Shakiba^{b,*}

- a Department Civil and Environmental Engineering, Princeton University, USA
- b Department of Aerospace Engineering Sciences, the University of Colorado Boulder, USA

ARTICLE INFO

Keywords: Thermo-chemical aging Effective crosslink density Large deformation Fracture Phase-field Finite-element

ABSTRACT

We propose a physics and chemistry-based constitutive framework to predict the stress and brittle failure responses of thermo-chemically aged elastomers. High-temperature aging in the presence of oxygen causes chemical reactions inducing significant changes in the elastomer macromolecular network. Experimental studies agree that the increase in effective chemical crosslinks is dominant, leading to increased material stiffness and ultimately causing brittle failure of aged elastomers. The main novelty of this work relies on directly connecting the evolution of the effective crosslink density to the mechanical properties which control stress and failure response of thermo-chemically aged elastomers. We equip the Arruda-Boyce hyperelastic constitutive equations to predict the stress-strain response until failure with phase-field to capture the induced brittle failure via a strain-based criterion for fracture. Four material properties associated with the stress and failure responses evolve to capture the detrimental effects of thermo-chemical aging. The evolution of the four material properties is characterized by the change in the effective crosslink density, obtained based on chemical characterization tests, for any given aging temperature and duration. The established constitutive framework is first solved analytically for the case of uniaxial tension in a homogeneous bar to highlight the interconnection between the four material properties. Then, the framework is numerically implemented within a finite element (FE) context via a user-element subroutine (UEL) in the commercial FE software Abaqus. The framework is validated versus a set of experimental results available in the literature. The comparison confirms that the proposed constitutive framework can accurately predict the stress-strain and failure responses of thermochemically aged elastomers. Further numerical examples are provided to demonstrate the effects of evolving material properties on the response of specimens containing pre-existing cracks exploiting the capabilities of the phase-field approach.

1. Introduction

During the last few decades, elastomers have shown to be extremely advantageous in a number of structural applications across multiple industries. During their service life, exposure to thermal loads in the presence of oxygen (i.e., thermo-chemical or thermo-oxidative aging) degenerates elastomers. Oxygen acts as a catalyst for the chemical aging of elastomers and ultimately leads to a progressive alteration of their chemical composition and degradation of their structural capacity (e.g., [1-7]). Therefore, it is imperative to investigate how elastomers respond to thermo-chemical degradation to better meet structural demands.

Oxygen can affect elastomer network through two main mechanisms: (i) oxygen diffusion for samples that are sufficiently thick, or (ii) homogeneous distribution for samples with a thickness of approximately 1 mm or smaller [1]. When test specimens are thin, there is

enough oxygen available and the aging process is not limited by diffusion [8]. In this study, we focus on sufficiently thin samples for which oxygen is homogeneously distributed and adopt the term thermochemical aging instead of thermo-oxidation to distinguish between the two scenarios mentioned above.

When an elastomer is subject to thermo-chemical aging, the relative rate of chain scission and crosslinking is essentially what determines whether the material becomes more ductile or more brittle [9]. The overall change in the effective crosslink density (i.e., density of elastically active or load-carrying chains) implicitly accounts for the resulting state of network configuration; that is, the resulting product of chain reaction kinetics activated by thermo-chemical aging. In most elastomers (e.g., natural rubber (NR) or styrene butadiene rubber (SBR)), while it is evident that some network chains inevitably undergo

E-mail address: maryam.shakiba@colorado.edu (M. Shakiba).

https://doi.org/10.1016/j.ijmecsci.2023.108721

Received 3 May 2023; Received in revised form 2 August 2023; Accepted 30 August 2023 Available online 9 September 2023 0020-7403/© 2023 Elsevier Ltd. All rights reserved.

Please cite this article Najmeddine, Shakiba. Mechanical as: Aimane Maryam International Journal Sciences.

https://doi.org/10.1016/j.ijmecsci.2023.108721

Corresponding author.

several episodes of scissioning, crosslinking reactions eventually dominate, resulting in an increase in effective crosslink density, particularly at longer aging times [3,9–11]. Increase in the effective crosslink density induces stiffening and embrittlement in elastomers [12–14].

Several researchers have developed analytical and numerical methods to predict the responses of chemically aged polymers (e.g., [3,11, 15-27]). These works, however, did not consider failure of elastomers due to thermo-chemical aging in their predictive efforts. To take fracture into account, Dal and Kaliske [28] proposed a micro-mechanical model based on a series of Langevin-type springs and a bond potential representing the inter-atomic bond energy acting on the chain. The authors used a micro-sphere description for scale transition and predicted the fracture in oxidized rubbers under biaxial loading. Volokh [29,30] introduced the energy limiter concept to limit the stored energy in aged elastomers when subjected to mechanical loading and therefore described the stress-strain and failure responses. Researchers also proposed an approach based on the intrinsic defect concept to predict the ultimate stresses and strains when thermo-oxidative aging is involved [31-35]. Abdelaziz et al. [34], Kadri et al. [36] used the stress limiter approach (and energy limiter approach) to predict the aging effects on stresses and strains at fracture for rubbers based on changes in molar mass (and concentration of elastically active chains and swelling ratio). However, situations for which complex crack patterns such as branching and coalescence might occur cannot be treated using the above formulations. Furthermore, the works described above lack a complete physics and chemistry-based description for the failure criteria and remain phenomenological. A more appropriate fracture approach that considers the underlying physio-chemical network changes due to thermo-chemical aging and can simulate complex brittle failure is thus needed for accurate predictions.

The phase-field approach, which was first introduced in Francfort and Marigo [37], has attracted increasingly more interest thanks to its capability to simulate complex quasi-brittle material responses [38-41]. More specifically, researchers utilized phase-field to simulate rateindependent crack propagation in rubbery polymers at large strains [42-46]. Kumar et al. [47,48] adopted the phase-field formulation to describe the nucleation and propagation of fracture and healing in elastomers under large quasi-static deformations. Integration of the phase-field approach within multi-physics conditions has also been investigated. Miehe et al. [49] proposed continuum phase-field models for brittle fracture towards fully coupled thermo-mechanical and multiphysics problems at large strains. Konica and Sain [50] employed the theory of transient networks to simulate reaction induced chainscission and crosslinking and coupled it with phase-field to simulate macroscale damage initiation and propagation in thermo-oxidatively aged polymers under mechanical stress. However, in their work, Konica and Sain [50] assumed linear functions for the change in the fracture properties to interpolate between unaged and completely aged conditions. These works did not establish a concrete physics-based mapping between the fracture properties involved in the constitutive framework and the physio-chemical changes manifested within the material during thermo-oxidation.

Miehe and Schänzel [42] used a micromechanically-motivated expression for the critical energy release rate in terms of the density of elastically active chains, the bond dissociation energy for a single monomer in a chain, and the number of monomers per chain based on the well-known [51] theory for unaged elastomers. However, such development has still not been addressed for aged elastomers. In addition to the critical energy release rate, the phase-field formulation takes as input another variable: an intrinsic length scale which acts as a regularization parameter dictating the width of a smeared crack. Discussion of the physical interpretation of the length scale in the context of pristine materials has been subject to debate. A few works have treated the length scale as a material property related to the strength of the material and argued that for the simple case of single-deformation states such as uniaxial tension, a strength-based criterion

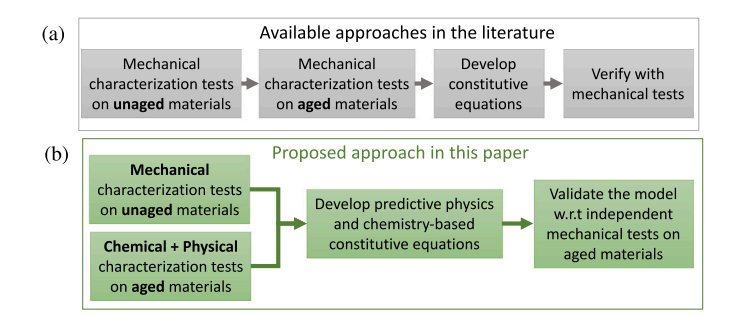


Fig. 1. (a) The procedure used in the literature to develop constitutive equations, and (b) the proposed procedure in this work to establish physics and chemistry-based constitutive equations for thermo-chemical aging in elastomers. Available approaches in the literature rely on mechanical tests on unaged and aged specimens to develop the constitutive equations, whereas, in the proposed approach in this work, we establish the constitutive equations based on mechanical tests on unaged and chemical and physical characterization tests on aged specimens.

for the initiation of fracture can be utilized [52–54]. However, it is unclear how material strength is quantitatively mapped to the underlying physio-chemical changes occurring within the elastomer when thermochemical aging is involved. An alternative criterion for the initiation of fracture that can be linked to the elastomer's network morphology (and thus can be monitored during aging) is the strain-based criterion similar to the one proposed by Miehe and Schänzel [42]. However, such development has still not been investigated.

In this work, we propose a physics and chemistry-based constitutive framework to predict the stress-strain and failure responses of thermochemically aged elastomers using the phase-field approach to fracture. In contrast to available constitutive frameworks, which rely on mechanical tests for both calibration and validation of the constitutive equations, we quantitatively connect our physical understanding and chemical measurements to the mechanical response and behavior of thermo-chemically aged elastomers. The general strategy commonly followed in the literature focuses on calibrating several material properties based on the mechanical responses of aged samples. Doing so usually introduces fitting variables that may or may not have any physical meaning. Instead, we establish a robust and efficient constitutive framework that connects the change in the material properties to the underlying physio-chemical changes and network alterations induced by thermo-chemical aging. Therefore, we bypass the need to calibrate the material properties and their evolution onto the aged mechanical responses. Fig. 1 schematically compares the available approaches in the literature versus our proposed framework in this work.

In particular, we first modify the energy stored in the bulk and the surface energy dissipated through fracture based on the changes in the network morphology of elastomers. We also use a strain-based criterion for crack nucleation. A natural byproduct of the strain-based criterion is the establishment of a direct relationship between the length scale, the strain at fracture, the material stiffness, and the critical energy release rate. The interconnection between the length scale and the other constitutive material properties makes it possible to examine its evolution during thermo-chemical aging as an intrinsic material property. We establish evolution functions for material properties which depend solely on chemically-measured quantities (i.e., the effective crosslink density measured using either the equilibrium swelling test, Nuclear Magnetic Resonance (NMR), Dynamic Flocculation Mode (DFM), Temperature Scanning Stress Relaxation (TSSR) measurements, or any other suitable chemical characterization technique). Consequently, the developed constitutive framework does not require additional fitting constants that do not carry physical meaning. The framework is validated versus available independent mechanical tests on thermo-chemically aged elastomers in the literature. This work, therefore, constitutes a clear contribution to the missing

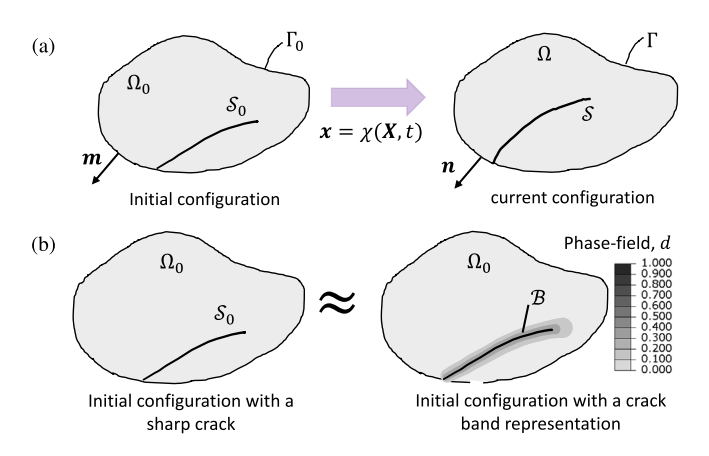


Fig. 2. (a) Geometric description of solid body undergoing fracture propagation in the initial (undeformed) and the current (deformed) configurations. (b) Substitution of a sharp crack discontinuity surface in a solid body, with a crack band as distribution of a continuous scalar phase-field, *d*, to describe the impact of fracture. *Source*: Adapted from [55].

quantitative relationship between the macromolecular changes and the mechanical and fracture responses induced by thermo-chemical aging within elastomers.

This manuscript is organized as follows. Section 2 summarizes the mathematical notations ascribed to kinematic quantities and presents the geometric description of a solid body undergoing fracture propagation. Section 3 describes the developed constitutive framework incorporating the effects of thermo-chemical aging on the coupled hyperelastic-phase-field response of elastomers. The solution of the developed framework for the case of a homogeneous one-dimensional (1-D) bar under uniform tension is explained in Section 4. Validation versus experimental data from the literature is presented in Section 5. Then, in Section 6, we discuss our results and present a few parametric studies on a single-edge notch sample aged for varying aging times. Finally, Section 7 concludes with some important remarks and ideas for subsequent future investigations.

2. Preliminaries

Tensorial notation is used in this work. Bold letters indicate a vector or a tensor. The inner product is represented by "·" and for any two tensors, $\mathbf{A} \cdot \mathbf{B}$, the summation is over the components of the right tensor (e.g., the inner product of two second-order tensors is $\mathbf{A} \cdot \mathbf{B} = tr(\mathbf{A}^T\mathbf{B})$, and for any two vectors, the product is $\mathbf{a} \cdot \mathbf{b} = \mathbf{a}^T\mathbf{b}$ where the superscript T indicates tensor or vector transpose). The time rate of change of a quantity in the material configuration (i.e., Lagrangian configuration) is known as a material derivative (D/Dt) and is indicated by a superimposed dot, whereas the time rate of change of a quantity in the spatial configuration (i.e., Eulerian configuration) is known as the spatial derivative $(\partial/\partial t)$ and is indicated by a prime sign. Additionally, Div and div represent the material and spatial divergence operators, respectively. Finally, $\nabla_{\mathbf{X}}(.) = \frac{\partial (.)}{\partial \mathbf{X}}$ and $\nabla_{\mathbf{x}}(.) = \frac{\partial (.)}{\partial \mathbf{x}}$ are the material and spatial gradient operators, respectively.

The problem solved in this work is formulated as follows. Consider an elastomeric body Ω_0 identified with the region of space it occupies within a fixed reference configuration as shown in Fig. 2(a). X presents the location of an arbitrary point in Ω_0 . Γ_0 is the boundary region of the body with the outward unit normal vector denoted by m. A smooth one-to-one motion mapping can subsequently be defined as $\mathbf{x} = \chi(\mathbf{X},t)$ giving the position of the point at the current configuration for a given time $t \in \mathbb{R}_+$ representing the temporal location (Fig. 2(a)). The deformation gradient can then be determined as $\mathbf{F} = \nabla_{\mathbf{X}}\chi(\mathbf{X},t)$. We also define the displacement field $\mathbf{u}(\mathbf{X},t)$ as the difference of the position vector in the reference configuration from the position vector

at the current configuration: $\mathbf{u}(\mathbf{X},\mathbf{t}) = \mathbf{x} - \mathbf{X}$. We assume that the solid medium is subject to specific body forces (per unit mass) $\bar{\mathbf{b}}$. Essential displacement boundary conditions, $\bar{\mathbf{u}}$, are prescribed on Γ_{0u} whereas natural boundary conditions are prescribed on Γ_{0t} such that $\Gamma_{0u} \cap \Gamma_{0t} = \emptyset$ and $\Gamma_{0u} \cup \Gamma_{0t} = \Gamma_0$. Additionally, we consider that the body Ω_0 contains a sharp crack S_0 that is smeared over a localization band $B \subseteq \Omega_0$ in which the damage field (or phase-field) $d(\mathbf{X},t)$ localizes (Fig. 2(b)). The diffuse damage band has an external boundary ∂B and unit outward normal \mathbf{m}_B . Correspondingly, essential phase-field boundary conditions are prescribed on ∂B_p while natural phase-field boundary conditions are prescribed on ∂B_p . The damage field takes real values between [0,1] in accordance with classical continuum damage mechanics principles where $d(\mathbf{X},t)=0$ refers to an intact material with no damage and $d(\mathbf{X},t)=1$ refers to a complete fracture.

3. Constitutive framework coupling hyperelasticity and phasefield for thermo-chemically aged elastomers

In this section, we present a detailed description of the proposed constitutive framework governing the response of thermo-chemically aged elastomers within the context of large deformation solid mechanics coupled with phase-field. Section 3.1 summarizes the governing differential equations for the problem (i.e., strong forms) and highlights equations describing phase-field. Section 3.2 presents the proposed approach to incorporate the changes in the macromolecular network due to thermo-chemical aging into the constitutive framework.

As argued in the Section 1, the literature agrees that although chain scission, crosslink breakage, and formation all happen simultaneously during the thermo-chemical aging of elastomers, crosslink formation eventually dominates, leading to an increase in the effective crosslink density, which in turn, results in an increase in the modulus and the hardening with embrittlement [9,12-14,56-58]. Therefore, in this study, we propose to connect the evolution of associated material properties to the macromolecular network to the effective crosslink density. We begin by summarizing the changes occurring in the material bulk hyperelastic energy, which was developed and validated in a previous work [25]. Then, we present our proposed approach to incorporate the evolution of the macromolecular network in the description of the critical energy release rate and the strain at fracture. The novelty of the current work lies in the addition of phase-field to predict fracture in thermo-chemically aged elastomers and how the material properties associated with fracture change by the alteration in the macromolecular network due to aging.

3.1. Governing differential equations

The set of governing partial differential equations to be solved in the initial configuration for a solid medium with evolving damage within the phase-field context are [42,59]

Div
$$(\mathbf{P}) + \bar{\mathbf{b}} = \mathbf{0}$$
 in Ω_0 and $\mathbf{Pm} = \bar{\mathbf{t}}$ on Γ_0 , (1)

$$\frac{G_c}{c_\alpha} \left(\frac{\alpha'_{(d)}}{l_c} - 2l_c \Delta_{\mathbf{X}} d \right) + \omega'_{(d)} \psi_{0(\mathbf{C})} = 0 \text{ in } B \subseteq \Omega_0 \quad \text{and}$$

$$\frac{2l_c G_c}{c_\alpha} \nabla_{\mathbf{X}} d \cdot \mathbf{m} = 0 \text{ on } \partial B_p$$
(2)

where $\mathbf{P}=2\mathbf{F}\frac{\partial \psi_{(\mathbf{C},d)}}{\partial \mathbf{C}}=\omega_{(d)}\mathbf{P}_0$ is the damaged first Piola–Kirchhoff stress tensor written in terms of $\omega_{(d)}$, a degradation function, and \mathbf{P}_0 its undamaged counterpart, $\psi_{(\mathbf{C},d)}$ is the damaged strain energy density function equal to $\psi_{(\mathbf{C},d)}=\omega_{(d)}\psi_{0_{(\mathbf{C})}}$ where $\psi_{0_{(\mathbf{C})}}$ is the undamaged strain energy density function, $\mathbf{C}=\mathbf{F}^T\mathbf{F}$ is the right Cauchy–Green strain tensor, $\bar{\mathbf{t}}$ is the applied traction boundary, $\alpha_{(d)}$ is the crack geometric function, G_c and I_c are the critical energy release rate and the length scale, respectively, and $c_\alpha=4\int_0^1\sqrt{\alpha_{(\beta)}}d\beta$. Note that the Cauchy stress

tensor can be calculated as $\mathbf{T} = J^{-1}\mathbf{P}\mathbf{F}^T$ where J is the determinant of \mathbf{F} .

Various versions of the phase-field approach exist in the literature depending on the choice of $\omega_{(d)}$ and $\alpha_{(d)}$. The more common version corresponds to the case for which $\omega_{(d)} = (1-d)^2$ and $\alpha_{(d)} = d^2$ [60–63]. In this version, damage begins to evolve at the onset of load application. An alternative version corresponds to the case for which $\omega_{(d)} = (1-d)^2$ but $\alpha_{(d)} = d$ [59,64]. This version of phase-field allows the material to develop elastically up to a certain critical strain level upon which fracture initiates.

Unaged elastomers (e.g., NR, SBR, etc.) show a purely nonlinear elastic response up until rupture. This means that damage is not allowed to commence until the material has reached a critical energy state wherein enough load-bearing chains have been broken causing nucleation of fracture. Moreover, under severe chemical aging scenarios which cause embrittlement, aged elastomers show an almost linear elastic response (under quasi-static loading at moderate strain rates) until they reach the critical level where they cannot sustain any more loads and fracture nucleates due to bond breakage. Therefore, we use the phase-field approach with a linear crack geometric function (i.e., $\alpha_{(d)} = d$). It must be noted that fracture can nucleate in a number of ways inside elastomers. As demonstrated through many experimental results, macroscopic crack nucleation can result from either one or all of the following fashions: (i) nucleation in bulk, (ii) nucleation from large pre-existing cracks, or (iii) nucleation from the boundary and small pre-existing cracks [47,48]. Fracture nucleation from large pre-existing cracks is well-captured by the phase-field approach (with $\alpha = d^2$); however, because such phase-field lacks the important consideration of material strength, it fails to describe crack nucleation in the bulk of smooth elastomers [47,48]. This limitation restricts the use of the phase-field approach to fracture problems dealing with uncut samples or samples with no pre-existing cracks. To overcome the restriction, in this work, we employ a strain-based criterion for fracture that allows us to conveniently describe crack nucleation in smooth elastomers [42]. The strain-based criterion is motivated by the physical understanding that, like all materials, elastomers are never perfect and contain inherent microscopic defects; thus, when a smooth elastomer is stretched monotonically, fracture nucleates at a given critical value of the applied stretch from one or more of these pre-existing defects.

3.2. Constitutive equations for thermo-chemically aged elastomers

This section presents the conjectured forms of the quantities required to solve the system of Eqs. (1) and (2) for a particular aging state. These quantities are the strain energy density function, the critical energy release rate, and the strain at fracture. We connect the macromolecular network alterations to the macroscopic properties through appropriate evolution functions for the material parameters involved in the constitutive framework.

3.2.1. Bulk hyperelastic energy

The modified Arruda–Boyce (AB) constitutive equations [65] to incorporate the effect of thermo-chemical aging is used in this work to describe the elastomer hyperelastic energy. The form of the strain energy density function taking into account the effect of thermo-chemical aging can be written as a function of the right Cauchy–Green strain tensor and the current state of aging, t_a , as follows [25]

$$\psi_{AB}\left(\mathbf{C}, t_{a}\right) = \mu_{(t_{a})} N_{(t_{a})} \left[\frac{\lambda_{\text{chain}(\mathbf{C})}}{\sqrt{N_{(t_{a})}}} \mathcal{L}^{-1} \left(\frac{\lambda_{\text{chain}(\mathbf{C})}}{\sqrt{N_{(t_{a})}}} \right) + \ln \frac{\mathcal{L}^{-1} \left(\frac{\lambda_{\text{chain}(\mathbf{C})}}{\sqrt{N_{(t_{a})}}} \right)}{\sinh(\mathcal{L}^{-1} \left(\frac{\lambda_{\text{chain}(\mathbf{C})}}{\sqrt{N_{(t_{a})}}} \right))} \right]$$
(3)

where

$$\mu_{(t_a)} = \mu_0 + \left(\rho_{(t_a)}^{cr} - \rho_0^{cr}\right) R\Theta \quad \text{and} \quad N_{(t_a)} = N_0 \frac{\rho_0^{cr}}{\rho_{(t_a)}^{cr}}$$
 (4)

where $\mu_{(t_a)}$ and $N_{(t_a)}$ are rubber modulus, and the number of Kuhn monomers per chain of the elastomer at the current state of aging t_a , respectively (given in Eq. (4). $\lambda_{\mathrm{chain}(C)} = \sqrt{\frac{I_{1(C)}}{3}}$ is the relative macro-stretch written as a function of the first invariant of the right Cauchy–Green strain tensor $I_{1(C)} = tr(C)$. $\mathcal{L}(\cdot) = \coth(\cdot) - \frac{1}{(\cdot)}$ is the Langevin function whose inverse \mathcal{L}^{-1} is given by several approximations in the literature and is equal to $\mathcal{L}^{-1}(x) = x\frac{3-x^2}{1-x^2}$ according to the Pade approximation for some $x \in \mathbb{R}$. μ_0 is the rubber shear modulus, N_0 is the number of Kuhn monomers per chain. ρ_0^{cr} and $\rho_{(t_a)}^{cr}$ are the crosslink densities of the unaged material (at aging time $t_a = 0$) and the aged material (at some later aging time t_a), respectively. R is the natural gas constant. Θ is the absolute temperature. Note that Eq. (3) can also be thought of as being a function of the effective crosslink density $\rho_{(t_a)}^{cr}$ since $\mu_{(t_a)}$ and $N_{(t_a)}$ are both implicit functions of $\rho_{(t_a)}^{cr}$. Moreover, in Eq. (4), the term $(\rho_a^{cr}) - \rho_0^{cr}$ gives the change in the effective crosslink density between the primary network configuration and the newly formed network configuration corresponding to some aging time t_a . Also, since the hyperelastic strain energy density function, Eq. (3), is a modification of the AB model, automatically a near-incompressible configuration is assumed in developing Eq. (3).

Eq. (4)₁ was developed and validated in [25] based on the fact that thermo-chemical aging causes the number of monomers per chain to decrease due to the formation of crosslinks between newly formed short-chains, which in turn induces more stiffness. On the other hand, the conservation of mass principle in polymers requires that the product of effective crosslink density and the number of Kuhn monomers per chain of the elastomer remain constant, motivating the derivation of Eq. (4)₂.

It must be noted that the AB constitutive equation was selected because an attractive feature of the AB description (besides being micromechanically motivated) is that it only requires two physics-based material properties, i.e., the network chain density (or equivalently the rubber shear modulus), and the number of Kuhn monomers to simulate elastomer behavior under various deformation states (i.e., uniaxial, shear, and biaxial) [65]. Therefore, the critical point is that since the AB model was proven to simulate the elastomers' behavior under uniaxial, shear, and biaxial deformation states, and the current modification for aging is micromechanically motivated, as long as the thermo-chemical aging occurs in a homogeneous manner, the developed constitutive equation in this work can capture the response of elastomers under any general deformation conditions in amorphous elastomers.

3.2.2. Critical energy release rate

This section focuses on the development of the critical energy release rate G_c for thermo-chemically aged elastomer. Treatment of G_c as an intrinsic material property in rubbers dates back to the work of Lake and Thomas [51]. Lake and Thomas [51] calculated the critical energy release rate in terms of the molecular structure of the elastomer. Their calculation was based on the statistical mechanics framework governing rubber elasticity. The theory is based on the dissociation energy of the bonds in the backbone of a monomer unit in a perfectly uniform network, U. A perfect network is defined as a network where all chains contain the same number of monomer units N_0 , and have the same displacement length as the mean end-to-end distance corresponding to a real network. In such a network, the critical energy release rate can be obtained by multiplying the energy required to rupture a chain, N_0U , by the number of chains crossing a unit area, $\frac{1}{2}\bar{r}n_0$, such that

$$G_c = \frac{1}{2}\bar{r}n_0N_0U$$
, where $\bar{r} = \sqrt{\frac{8N_0}{2\pi}}l$ (5)

where \bar{r} is the mean end-to-end distance of an ideal chain containing N_0 monomer units each of length l. The presented mean end-to-end distance can be calculated from the theory of rubber elasticity assuming

Gaussian statistics for the probability density per unit volume of a randomly jointed chain [51]. Substituting \bar{r} into Eq. (5), yields

$$G_c = \sqrt{\frac{2}{3\pi}} n_0 l N_0^{\frac{3}{2}} U \tag{6}$$

which is the final form of a micromechanically motivated Griffith-type criterion for an unaged elastomer.

To account for thermo-chemical aging effects, we first note that the expression of G_c derived herein is written as a function of the number of monomer units. In the AB description, this parameter corresponds to the number of Kuhn monomers, which was derived earlier as a function of the effective crosslink density (i.e., Eq. (4)₂). Additionally, the number of chains per unit volume can also be conveniently written as a function of the effective crosslink density using the expression $n(\rho^{cr}_{(t_a)}) = \rho^{cr}_{(t_a)} \mathcal{N}_A$ where \mathcal{N}_A is Avogadro's number. We eventually arrive at an expression of critical energy release rate for different aging conditions, $G_c(t_a)$, written entirely in terms of the effective crosslink density $\rho^{cr}_{(t_a)}$, the dissociation energy of a single bond U, and the length of a monomer unit I, that is

$$G_{c}(t_{a}) = \sqrt{\frac{2}{3\pi}} \rho_{(t_{a})}^{cr} \mathcal{N}_{A} l(N_{(t_{a})})^{\frac{3}{2}} U$$
 (7)

The expression derived above for G_c represents as an evolution function for the critical energy release rate given in terms of the effective crosslink density achieved at a certain aging state during thermochemical aging.

Note that in the evolution function of G_c , the value of the dissociation energy of the bonds in the backbone of a monomer, U, is a known value. It can be taken as the average dissociation energy of all bonds in the backbone of the monomer in a similar fashion to that followed in the work of Song et al. [66]. For a single monomer, U can be obtained by dividing the average molar dissociation energy (which is given in unis of (energy/moles)) by Avogadro's number. This leaves the length of a monomer unit, I, to be the only unknown physical parameter in the expression of G_c . The length of a monomer unit, I, is considered to be constant for all aging times and is therefore determined based on the G_c corresponding to the unaged state.

3.3. Strain-based criterion for fracture of thermo-chemically aged elastomers

In this work, we employ a strain-based criterion for fracture nucleation in smooth specimens (i.e., specimens containing no large precracks). The version of the phase-field approach adopted in this work (which was presented in Section 3.1) allows for an elastic regime up to the onset of crack nucleation. Such a formulation is attractive as it provides the ability to construct criteria with thresholds for fracture initiation and nucleation. Particularly, it allows us to construct an energetic criterion with a threshold based on the limiting strain, i.e., the strain at fracture.

We propose to express the evolution of the engineering strain at fracture in terms of the effective crosslink density (or equivalently the number of Kuhn monomers since the two quantities are related through Eq. (4)₂). Motivated by the findings of Bueche and Halpin [67],Smith [68] who showed that the stretch at fracture can be explicitly formulated as a function of the inverse square root of the crosslink density, we propose to modify the derived expression for stretch and write that the strain at fracture at a given aging time t_a is given by $\varepsilon_{b_{(t_a)}} = C \left(\frac{1}{p_{(t_a)}^{cr}}\right)^{3/2}$ where C is a constant of proportionality. Since $\varepsilon_{b_{(t_a)}}$ must be equal to ε_{b_0} (the strain at fracture corresponding to the unaged state), we find that the constant C is given by $C = \varepsilon_{b_0}(\rho_0^{cr})^{3/2}$. Thus, we finally reach the following expression for the evolution of the strain at fracture

$$\varepsilon_{b_{(t_a)}} = \left(\frac{\rho_0^{cr}}{\rho_{(t_-)}^{cr}}\right)^{3/2} \varepsilon_{b_0} = \left(\frac{N_{(t_a)}}{N_0}\right)^{3/2} \varepsilon_{b_0} \tag{8}$$

The assumption that the strain at fracture can be linked to the number of Kuhn monomers stems from the understanding that as rubber chains become smaller and more rigid, there is more potential for them to break and therefore the strain at fracture is expected to decrease. Note that Eq. (8) is self-contained and does not include any fitting variables. We shall see an example of the predicted strain at fracture versus experimental data in Section 5.1.

The procedure followed to validate the proposed framework and obtain the material properties involved in this work is illustrated in Fig. 3.

A summary of the simplifying assumptions is listed here. The crosslinking mechanism is the dominant phenomenon in the thermochemical aging of elastomers and the energy dissipation, and the effects of dangling chains are neglected. The chains forming the elastomer are all perfectly uniform, meaning they all contain the same number of monomer units and have the same displacement length as the mean for a real network. The elastomer is saturated with oxygen, and the energy due to chemical diffusion can be neglected. The chemical reactions associated with oxidation occur homogeneously inside the thin samples. Temperature does not change locally upon the application of mechanical loading or is negligible. The material is assumed incompressible and isotropic. The aging process does not depend on the strain. It must be noted that most of these assumptions are common among all the constitutive equations, which were developed to simulate thermo-chemical aging in elastomers in the literature (e.g., [3,20,69]). Moreover, the developed constitutive framework in this work can be incorporated into the more complicated diffusion-reaction-based constitutive equations to be fully coupled with the diffusion equations. For example, the strain energy density function presented herein, which is implicitly a function of the extent of reactions, can be used instead of the assumed mechanical Helmholtz free energy in the diffusion and reaction-driven work of [22]. In such cases, where we solve a set of partial differential equations to calculate the effective crosslink density as a function of oxygen and time, the established framework herein can automatically be used to simulate cases of partial oxygen saturation and heterogeneous and diffusion-limited thermo-chemical aging.

We reiterate that contrary to the existing works, we do not fit the constitutive framework onto the *aged* experimental stress–strain curves. Instead, the relevant material properties evolve in terms of the effective crosslink density during thermo-chemical aging. The effective crosslink density can be obtained based on a suitable chemical characterization test (e.g., equilibrium swelling test, NMR, DFM, TSSR, etc.) for any desired aging time and temperature. As such, the evolution functions do not contain any extra fitting parameters that lack physical meaning; rather, they are simply expressed in terms of the inputs which are: evolving effective crosslink density for a given aging temperature and time, and the material properties of the *unaged* configuration. To further clarify this procedure, Section 4 derives the analytical solution of the developed framework for the case of a 1-D bar and presents the steps to be taken to predict the aged material responses.

4. Homogeneous case of bar under uniform tension

This section presents the analytical derivation of the proposed framework for a 1-D bar. The present derivation serves to highlight the various steps involved in arriving at the complete stress–strain response of an aged sample from the onset of load application to complete fracture.

Let us consider a homogeneous bar involving a near-incompressible and isotropic hyperelastic solid. It is assumed the bar has been thermochemically aged for varying periods of time and subsequently loaded under uniaxial tension. In this case, the deformation gradient is expressed as a function of the applied uniaxial stretch λ as follows

$$\mathbf{F}(\lambda) = \begin{pmatrix} \lambda & 0 & 0 \\ 0 & \frac{1}{\sqrt{\lambda}} & 0 \\ 0 & 0 & \frac{1}{\sqrt{\lambda}} \end{pmatrix} \tag{9}$$

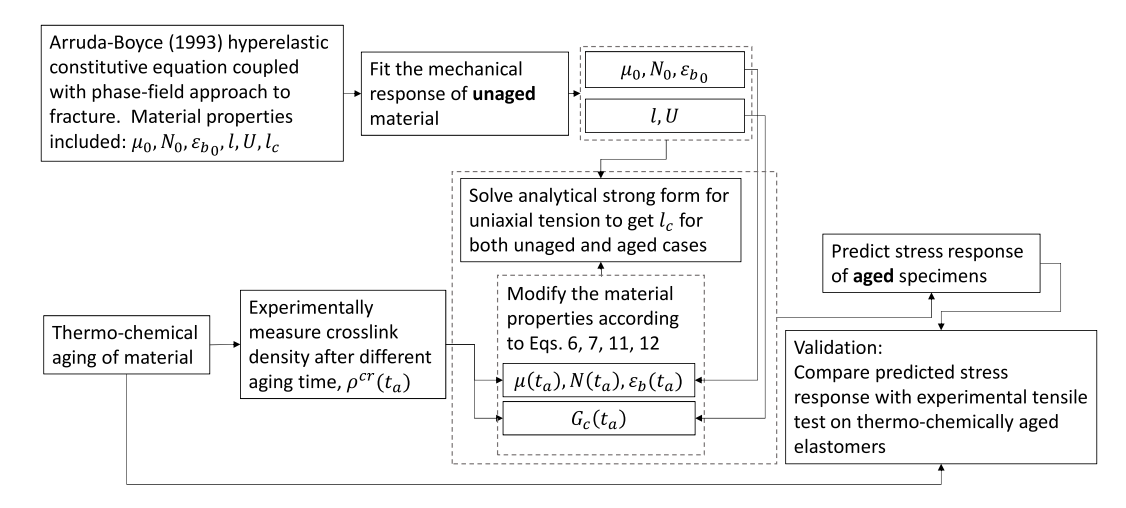


Fig. 3. Procedural flowchart for the identification of the material properties and the prediction and validation of the constitutive framework. The material properties associated with unaged mechanical hyperelastic and fracture response are taken from a tensile test. The evolution of a crosslink density after different thermo-chemical aging times is acquired from chemical characterization tests. The mechanical properties are then modified and used to predict the mechanical response of thermo-chemically aged elastomer.

The left Cauchy-Green strain tensor can be written as

$$\mathbf{C}(\lambda) = \mathbf{F}(\lambda)^T \mathbf{F}(\lambda) = \begin{pmatrix} \lambda^2 & 0 & 0 \\ 0 & \frac{1}{\lambda} & 0 \\ 0 & 0 & \frac{1}{\lambda} \end{pmatrix}$$
(10)

whose first invariant is given by $I_{1_{(\lambda)}} = tr(\mathbf{C}) = \frac{2}{\lambda} + \lambda^2$.

Eq. (3) can be written in polynomial form using the first five terms of the inverse Langevin function as

$$\psi_{AB}(\mathbf{C}, t_a) = \mu_{(t_a)} \sum_{i=1}^{5} c_i \frac{1}{N_{(t_a)}^{2i-2}} \left(I_{\mathbf{1C}}^i - 3^i \right)$$
 (11)

where the constants c_i in Eq. (11) are equal to $c_1 = \frac{1}{2}, c_2 = \frac{1}{20}, c_3 = \frac{11}{1050}, c_4 = \frac{19}{7000}, c_5 = \frac{519}{673750}$, and $\mu_{(t_a)}$ and $N_{(t_a)}$ are given by Eq. (4). In the case of uniaxial tension, Eq. (11) can be expressed as a

In the case of uniaxial tension, Eq. (11) can be expressed as a function of the applied stretch as

$$\psi_{AB}(\lambda, t_a) = \mu(t_a) \sum_{i=1}^{5} c_i \frac{1}{N(t_a)^{2i-2}} \left(I_1(\lambda)^i - 3^i \right)$$
 (12)

Therefore, the first Piola–Kirchhoff stress in uniaxial tension P can be computed as

$$P(\lambda, t_a) = \frac{\partial (\psi_{AB}(\lambda, t_a))}{\partial \lambda} \tag{13}$$

For the case of homogeneous damage state, $\Delta d = 0$ (i.e. damage is uniform in the bar) and Eq. (2)_a becomes

$$\omega'_{(d)}\psi_{AB}(\lambda, t_a) + \frac{G_c \alpha'_{(d)}}{l_c c_a} = 0$$
 (14)

Note that for the version of the phase-field employed in this work, the first derivatives of the degradation and the crack geometric functions with respect to the phase-field variable are given by $\omega'_{(d)}=2(d-1)$ and $\alpha'_{(d)}=1$, respectively, while c_{α} is given by $c_{\alpha}=4\int_{0}^{1}\sqrt{\alpha_{(\beta)}}d\beta=\frac{8}{3}$. Eq. (14) is the balance equation for the phase-field variable govern-

Eq. (14) is the balance equation for the phase-field variable governing the evolution of the damage field inside the bar. The phase-field variable d can be solved either analytically or numerically provided that all necessary inputs are known. These inputs are: the effective crosslink density $\rho_{(l_a)}^{cr}$ for a given aging time and temperature, the critical energy release rate $G_{c(l_a)}$ corresponding to said crosslink density, and the length scale l_c . The length scale depends on the material stiffness and its fracture resistance, thus also implicitly on the effective crosslink density, as shown through Eq. (14).

To see how the length scale can be determined for a given aging time t_a , let us simplify Eq. (14) by substituting $\alpha_{(d)}$, $\omega_{(d)}$, and c_{α} terms.

We obtain

$$\psi_{AB}(\lambda_{b_{(t_a)}}, t_a) - \frac{3G_{c(t_a)}}{16I_c} = 0 \tag{15}$$

where $\lambda_{b_{(l_a)}}$ is the stretch at failure given by $\lambda_{b_{(l_a)}} = \varepsilon_{b_{(l_a)}} + 1$. Note that the value d=0 was substituted for the phase-field variable since fracture will nucleate when d ceases to be identically 0. Thus, for a particular value of the effective crosslink density, $\psi_{AB}(\lambda_{b_{(l_a)}}, t_a)$ and $G_{c(l_a)}$ can be determined using Eqs. (12) and (7), respectively, and Eq. (15) can be solved for the only unknown parameter l_c .

5. Validation of the developed constitutive framework

In this Section, we validate the proposed framework versus the experimental work reported by Rezig et al. [35] for the cases in which aging was performed at 90 °C and 100 °C. Rezig et al. [35] conducted a series of experimental studies on the thermo-chemical aging effects in filled SBR. The authors determined the crosslink densities and stress-strain responses corresponding to unaged and aged SBR under a series of temperatures for various aging times ranging from 0 to 60 days.

First, the material properties associated with the unaged configuration were obtained by fitting the unaged version of the constitutive framework to the stress responses of the unaged SBR reported in [35]. By fitting to the stress–strain curve, μ_0 , N_0 , and ϵ_{b0} were calibrated. G_c for the unaged material was selected equal to 24 N/mm which is typical for filled SBR elastomers [70]. The average dissociation energy of all bonds in the backbone of the monomer, U, was calculated in a similar fashion to the work of Song et al. [66] and a value of $5.74\times10^{-19}~J$ was used. At this stage, Eq. (2)a (or equivalently for the case of uniaxial tension Eq. (15)) can be solved for the only left unknown parameter l_c . These four material properties associated with unaged SBR are presented in Table 1 and are the only fitting we conduct in this work.

Once the unaged material properties were obtained, their evolution according to the proposed evolution functions (i.e., Eqs. (4), (7), and (8)) can be acquired for any aging time based on the reported effective crosslink density. For example, let us consider the case in which the material was thermally aged for $t_a=45$ days under $100\,^{\circ}\mathrm{C}$. Substituting the crosslink density associated with $t_a=45$ in Eq. (7) to obtain $G_{c(t_a)}$ and in Eq. (12) to obtain $\rho_0\Psi_{AB}(\lambda_b,t_a)$, we can solve for l_c in Eq. (15) with $\lambda_b=\varepsilon_{b(t_a)}+1$ for the case of a tensile test. The procedure can be extended to the remaining aging times and the l_c corresponding to each aging state can be calculated in a similar fashion. Tables 2 and 3 present the values for all the material properties evolving due to aging obtained for the various aging times considered under $90\,^{\circ}\mathrm{C}$ and $100\,^{\circ}\mathrm{C}$, respectively.

Table 1

Material properties of unaged SBR obtained by fitting to the mechanical response and crosslink density of pristine material reported in [35].

Rubber modulus μ_0 (MPa)	Number of Kuhn monomers N_0	Critical energy release rate G_c (N/mm)	length scale l_c (mm)
0.8	85	24.0	0.075

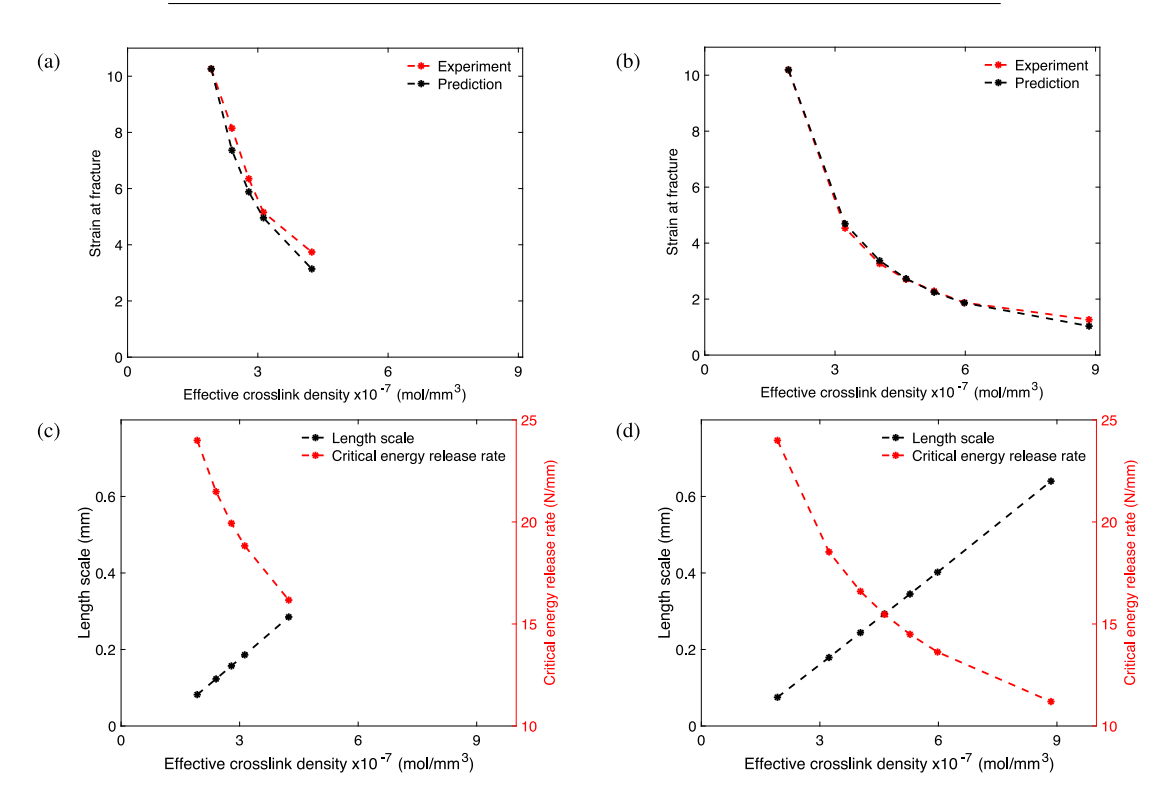


Fig. 4. Comparison between the evolution of the strain at failure for SBR as measured experimentally in [35] and the prediction using Eq. (8) when the material was aged at: (a) 90 °C; and (b) 100 °C. Evolution of the computed length scale I_c and the critical energy release rate G_c as a function of the effective crosslink density (obtained using Eq. (7)) when the material was aged at: (c) 90 °C; and (d) 100 °C.

As examples, the evolution of strain at fracture, length scale, and critical energy release rate are plotted in Fig. 4. Figs. 4(a) and 4(b) present the predicted strain at fracture (obtained based on Eq. (8)) and experimental strain at fracture values as a function of the effective crosslink density for the two aging temperatures of 90 °C and 100 °C, respectively. It is evident that a perfect match between experiment and prediction based on Eq. (8) is obtained. The perfect observed match confirms the form of the evolution function proposed in Eq. (8). Moreover, the accuracy associated with strain at fracture prediction allows accurate determination of the length scale evolution. Further validation example of the prediction of strain at fracture versus experimental work of Hamed and Zhao [10] is presented in Appendix C.

The resulting G_c and consequently I_c values are plotted as a function of the effective crosslink density in Figs. 4(c) and 4(d) for the two aging temperatures. Interestingly, I_c is found to evolve linearly with respect to the effective crosslink density for both aging temperatures, whereas G_c , on the other hand, decreases with increasing effective crosslink density as is expected for both aging temperatures. The linear increase for I_c suggests that the length scale, similarly to the effective crosslink density, possibly evolves in a sigmoidal manner with respect to aging time. It must be noted that the length scale parameter changes as a function of aging time, and therefore, the fracture process zone varies in thermo-chemically aged elastomers depending on the aging condition (i.e., time and temperature) that the material has been subjected to. It is observed previously that the rate of increase of crosslink density as a function of aging is slow at the start, then it increases by aging, before it decreases again as the available radicals for crosslinking are consumed

at longer aging times [71]. This finding is crucial as it sheds light on the evolution of an important parameter in the phase-field characterization of damage in thermo-chemically aged elastomers.

Having obtained all the material properties, Eqs. (1) and (2) can be solved for the damage and stress fields for the problem in hand. The full stress–strain response – including failure – of thermo-chemically aged elastomers can then be predicted. The predictions are reported in the following subsections.

5.1. Homogeneous solution

This section presents the analytical solution corresponding to the case of an isotropic, near-incompressible elastomeric bar which was thermo-chemically aged and subsequently loaded under uniform tension. The aged material properties presented in Tables 2 and 3 are used to plot the engineering stress–strain response corresponding to each particular aging time at each aging temperature.

Figs. 5(a) and 5(b) show the predictive capability of the developed framework at 90 °C and 100 °C, respectively. A very good match between the experimental results and the stress–strain curves calculated using the present approach is achieved for both aging temperatures. Fig. 5 validates the capability of the developed framework in predicting the stress–strain response of thermo-chemically aged elastomers. The sharp drop in stress characterizing post-failure response cannot be captured in the homogeneous solution; therefore, in the next section, the finite element (FE) solution and full validation are presented.

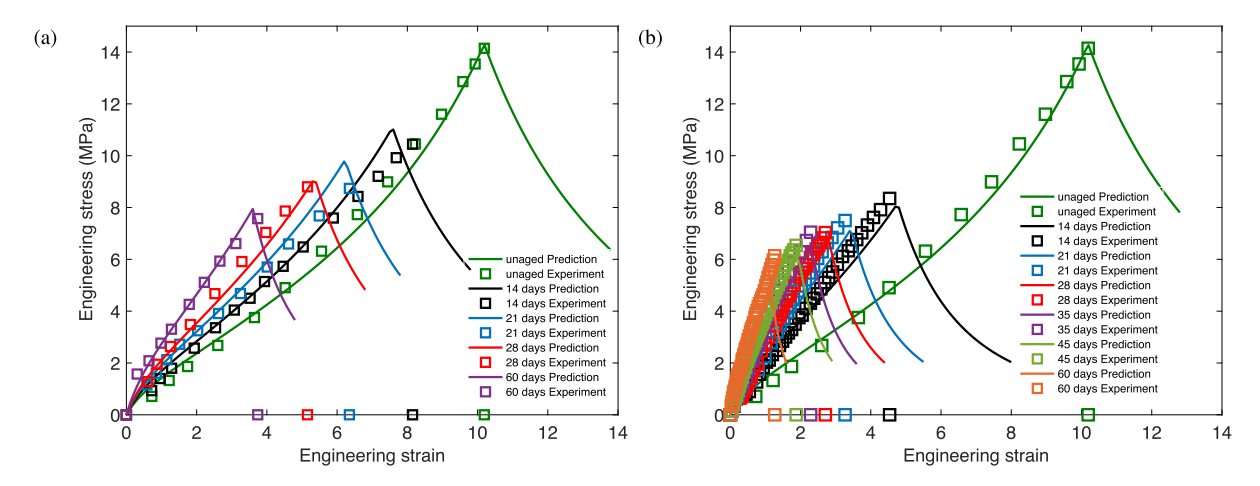


Fig. 5. Predictions of the stress–strain response using the developed constitutive framework for the case of analytical derivations of a 1-D bar under uniaxial tension verified against the experimental results for an SBR material aged at (a) 90 °C, and (b) 100 °C. The proposed framework can capture the stress–strain response up to failure and failure of the thermo-chemically aged SBR for different aging durations and temperatures. Experimental data are obtained from [35].

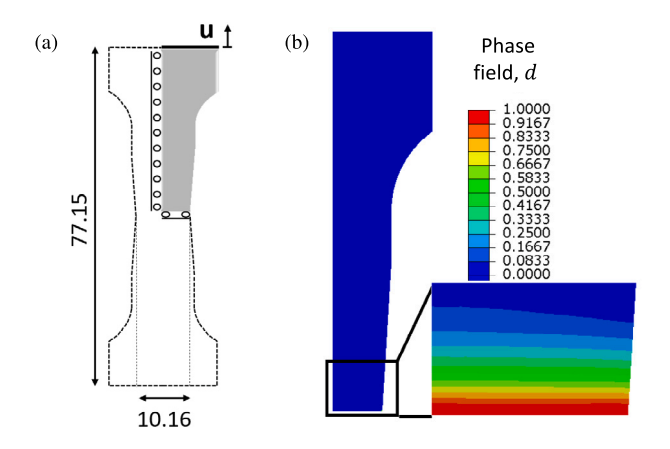


Fig. 6. (a) Sample geometry used in the FE simulations. All dimensions are given in mm unit. For the sake of minimizing the computational cost, only a quarter of the geometry was used and symmetric boundary conditions were applied on the left and bottom edges of the upper rightmost quarter; (b) contour plot for the phase-field damage variable for an SBR material thermally aged for 45 days at 100 °C.

5.2. Finite element solution

This section discusses the FE solution of the response of a dumbbellshaped thermo-chemically aged sample axially loaded in tension by a prescribed deformation u (Fig. 6(a)). We focus on two cases for which the material was aged for 45 and 60 days under 100 °C. Details of the FE implementation of the present constitutive framework are attached in Appendix A. The FE simulations were performed on the FE software Abaqus [72] via a user-element subroutine (UEL) within a two-dimensional (2-D) context. In all simulations, the element size was taken to be $l_c/4$ and plane strain quadrilateral elements were used. The system of governing differential equations was solved using the staggered solution algorithm proposed by Miehe et al. [73]. To minimize the computational cost associated with the FE simulation, only a quarter of the geometry was used and symmetric boundary conditions were applied on the left and bottom edges as shown in Fig. 6(a). The material properties for the case $t_a = 45$ and 60 days (see Table 3) were used to run the simulations.

Moreover, Fig. 6(b) illustrates a sample contour plot for the phase-field damage variable for $t_a=45$ days aging case highlighting the critical region which experiences extreme damage. Note that the width of the diffuse damage band is governed by the value of l_c . For this case, l_c was found to be 0.179 mm. This is approximately 0.24% of

the specimen dimension. As pointed out in [74], when the length scale is considered as a material constant (which is the case for the present study) and is small with respect to the dimensions of the sample, both the peak load as well as the damage contour can be very well captured using the phase-field approach adopted here. In this work, we have shown that the obtained l_c values for the varying aging times increases linearly with respect to the effective crosslink density, and thus in a sigmoidal manner with respect to aging time. It is thus expected that the length scale would reach a plateau at some maximum aging time. It remains to evaluate whether damage patterns would provide any meaningful conclusions for cases where l_c approaches such limit.

Figs. 7(a) and 7(b) demonstrate the comparison between the stressstrain responses using the present framework (obtained both analytically and numerically on Abaqus) and the corresponding experimental response for the cases of $t_a = 45$ and 60 days, respectively. It can be seen that the framework can predict the responses of both aging times with very high accuracy. Particularly, the increased stiffness due to thermo-chemical aging, the peak stress reached within the aged material, and the strain at fracture linked to the change in the number of monomer units per chain are all shown to match highly accurately with the experimental response for both aging states. In fact, treating the length scale as intrinsic material property and relating the changes in the critical energy release rate and the strain at fracture to the evolution of the effective crosslink density has proven to be vastly efficient in capturing the full stress-strain response of the thermochemically aged elastomers. The highly predictive capability of the proposed constitutive framework makes the present effort especially attractive as it combines our understanding of how thermo-chemical aging affects the macromolecular structure of the network and the adaptability of phase-field approach to simulate brittle fracture.

6. Discussion and parametric studies

In this section, we discuss the effects of aged material properties on the response of specimens containing pre-existing cracks. In particular, we investigate the case of a thermo-chemically aged single-edge notch specimen loaded under uniaxial tension as shown in Fig. 8(a) (note that the specimen size is 1×1 mm). We assume that the specimen underwent the exact same aging procedure reported in the work of Rezig et al. [35] under $100\,^{\circ}\text{C}$ and therefore the evolution of the effective crosslink density yields the exact same material properties highlighted in Table 3. We ran two simulations corresponding to two different aging states: 45 and 60 days.

Fig. 8(a) illustrates the load-displacement curves corresponding to the two aging states. At first glance, the figure demonstrates that

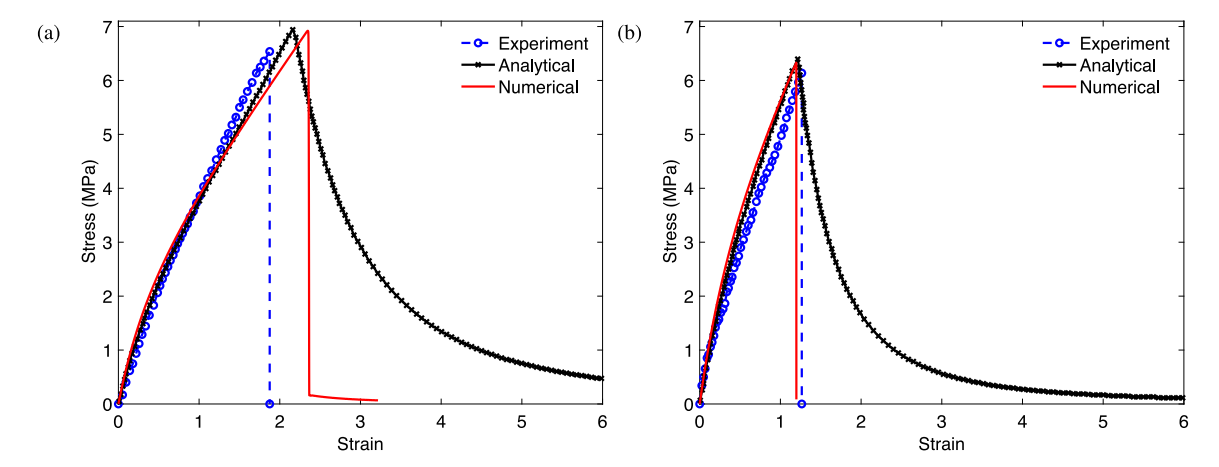


Fig. 7. Comparison between the stress-strain and failure responses using the present framework (obtained both analytically and numerically on Abaqus) and the experimental results for an SBR thermally aged for (a) 45 days and (b) 60 days at 100 °C. (The experimental results are taken from [35].)

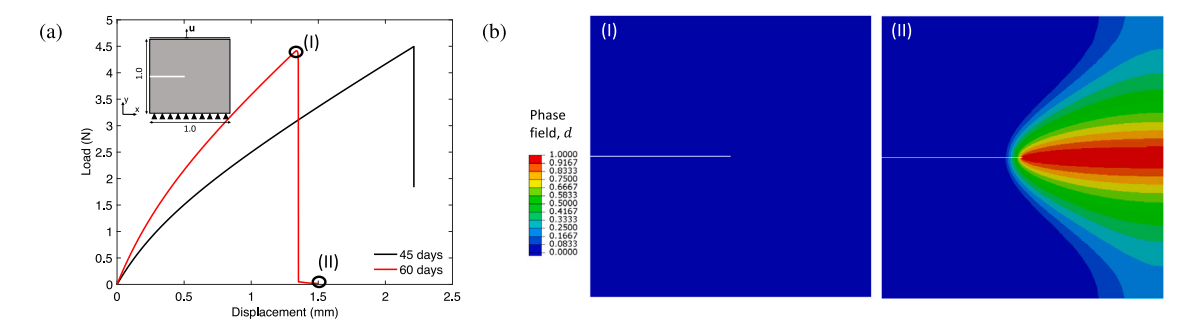


Fig. 8. (a) Load–displacement plots corresponding to single-edge notched SBR materials that have been thermo-chemically aged for two aging times (i.e., 45 and 60 days) at 100 °C and subsequently loaded in tension by a prescribed displacement u (dimensions are given in mm unit), and (b) phase-field contours at the two points marked on the load–displacement plot for the sample that was aged for 60 days.

the developed framework can accurately predict aging effects on the response because (1) both the maximum load and the displacement at failure decrease with an increase in aging time, and (2) the stiffness increases with increasing aging time, as one would correctly expect. In general, the observed behavior for the two aging times is expected. Specifically, the decrease in maximum load and displacement at failure is governed by the evolution of the critical energy release rate which was shown to decrease with respect to aging time according to Eq. (7). The decrease in the critical energy release rate is itself due primarily to the fact that the number of Kuhn monomers decrease over aging time. Therefore, the premature fracture of thermo-chemically aged elastomers is directly linked to the decrease in the monomer density per chain. This observation implies that in the aged elastomer, a newly formed network containing shorter chains (albeit more rigid) compared to the original unaged network is continuously formed. On the other hand, the rise in stiffness is expected since the newly formed network contains a denser and a more crosslinked chain coil. In other words, while the chains in the aged elastomer are smaller and contribute to premature failure, the increase in effective crosslink density affect the stiffness and causes the material to undergo embrittlement.

Fig. 8(b) shows the evolution of the corresponding phase-field contour at two points along the load–displacement curve as shown in Fig. 8(a). The effect of the length scale as a material parameter is clearly demonstrated through the width of the crack band as the latter grows during the simulation. Though, due to the large value of the length scale for the present case, the width of the smeared crack appears to be rather large compared to the specimen's dimensions.

Therefore, with the version of the phase-field employed in this work, physical interpretation of the size of the crack band (or equivalently the damage pattern) is to be approached with care when the length scale is large with respect to the specimen's dimensions. Again, this

observation has been pointed out in the work of Mandal et al. [74] who confirmed that when the present phase-field version is employed, damage patterns only provide meaningful insight when the length scale is small with respect to the specimen's dimensions. It should be noted that the present case is merely illustrative and therefore the dimensions of the sample (i.e., 1×1 mm) do not provide practical meaning other than what we have intended it to be (a parametric case). Nonetheless, the load–displacement curve presented in Fig. 8(a) correctly highlights the sudden drop and brittle fracture response that is typically observed for the single-edge notch example when loaded under uniaxial tension.

To better assess the influence of length scale relative to the specimen's dimensions, we opted to magnify the single-notch edge specimen by a factor of 20, resulting in a size of 20 × 20mm, as presented in Fig. 9a. We ran a simulation corresponding to the 60-day aged sample and examined the evolution of the crack band. Fig. 9b and c present the load-displacement curve and corresponding contour evolution of the phase-field variable at six points along the load-displacement plot, clearly highlighting the appropriateness of the newly considered sample size relative the value of the length scale at this particular aging time (i.e., $l_c = 0.640$ mm). The size of the damage band appears to be rather small compared to the one previously calculated for the 1×1 mm specimen considered in Fig. 8(a). Additionally, the new specimen size preserves the key features in the load-displacement plot which were previously observed for the smaller specimen size, namely, the presence of a purely elastic range up until a critical strain energy level, followed by a sharp drop in force once the crack has sufficiently progressed and enough load bearing chains have been broken due to the highly aged chain network morphology. Movies illustrating the evolution of both the phase-field contours as well as the T22 Cauchy stress profile have been appended as supplementary material to the manuscript. It is therefore evident that by increasing the size of the specimen,

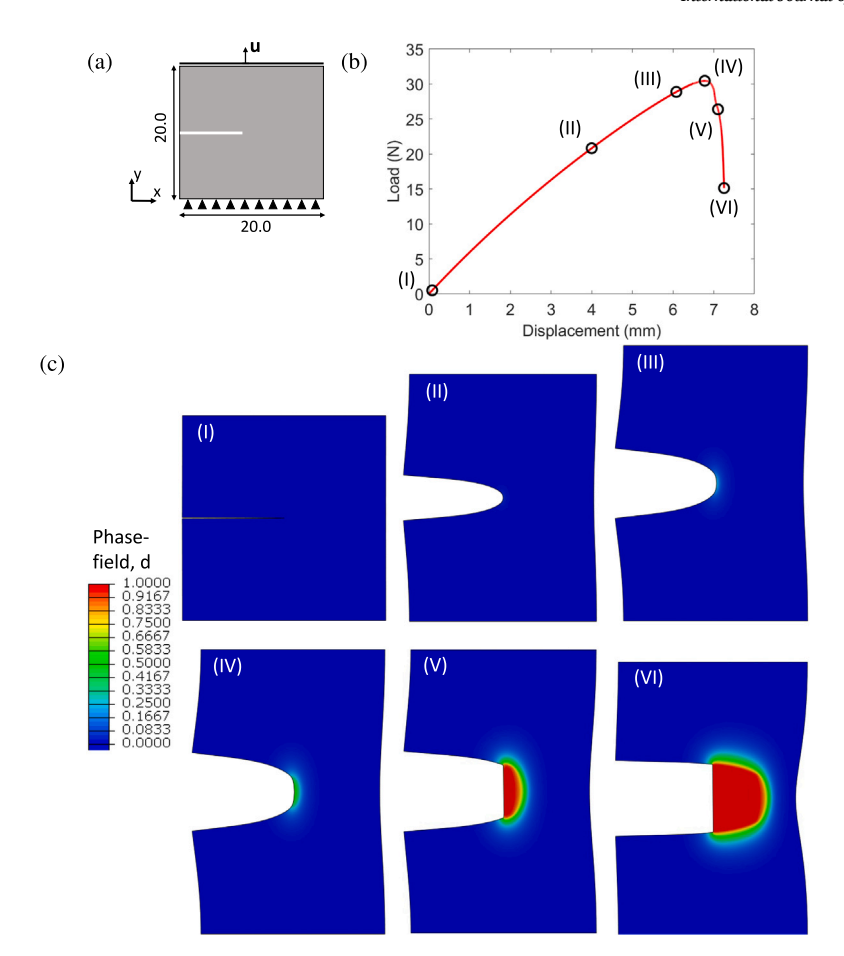


Fig. 9. (a) The schematic representation of a single-edge notched specimen, applied boundary conditions, and prescribed displacement u (dimensions are given in mm unit), (b) the load–displacement curve associated with the presented specimen for an SBR material that had been thermo-chemically aged for 60 days at $100\,^{\circ}$ C and subsequently loaded in tension, and (c) the evolution of phase-field corresponding to points (I) to (VI) on the load–displacement curve (scale factor $\times 1$).

considerations related to the meaningfulness of the length scale – and consequently, the size of the crack band – are appropriately addressed.

7. Conclusions

A physics and chemistry-based and thermodynamically consistent constitutive framework to predict the failure responses of thermochemically aged elastomers is developed. The constitutive framework combines our understanding of how thermo-chemical aging affects the macromolecular structure of the rubber network and the adaptability of the phase-field approach to simulate brittle fracture. The effect of thermally-driven crosslinking processes in modifying the bulk hyperelastic energy and the dissipated energy through fracture is considered. Therefore, the framework provides a quantitative approach linking our previously known understanding of macromolecular changes to the mechanical responses of thermo-chemically aged elastomers. Specifically, we showed that the evolution of the AB hyperelastic strain energy density function (which is characterized by two micromechanicallymotivated material properties: rubber modulus and the number of Kuhn monomers), the critical energy release rate, the strain at fracture, and the length scale can be predicted entirely in terms of a single physiochemical quantity: effective crosslink density. The framework uses the results of a mechanical test on unaged SBR, and a chemical characterization test on aged SBR under different aging conditions to predict the mechanical responses of aged SBR. Therefore, the framework has predictive capabilities and is independent of the mechanical tests on aged elastomers.

In particular, first, the interconnection between relevant material properties was discussed analytically for the case of 1-D uniaxial tension. Second, it was shown that the length scale variable characterizing

phase-field based damage can be treated as an intrinsic constitutive material property and fracture nucleation in thermo-chemically aged elastomers can be captured conveniently through a strain-based criterion for crack initiation. The framework was subsequently implemented numerically through a user-element subroutine (UEL) on the FE software Abaqus to simulate more complicated geometries within a 2-D context. The proposed framework was shown to predict the mechanical responses of thermo-chemically aged elastomers independently of any mechanical tests on the aged samples with very high accuracy. Such development is unprecedented in the literature particularly as the proposed framework is fairly simple and requires very few material parameters whose evolution during thermo-chemical aging can be connected directly to the evolving chain network characterized by the effective crosslink density.

It is worth reiterating that in developing the proposed constitutive framework, homogeneous oxidation through sample thickness was assumed following [9]'s argument on the interconnection between sample thickness and aging temperature. Additionally, it was also assumed that the *effective* crosslink density implicitly accounts for all underlying complex dissipation mechanisms (e.g., chain scission, crosslinking, chain breakage, etc.) that happen at the nanoscale within elastomer network due to aging. Further experimental data is needed to verify if the crosslink formation remains dominant for higher aging temperatures and longer aging duration, where elastomers may be used in more extreme conditions in the future. It also remains to examine the relevant modifications to the proposed framework for cases where viscoelastic effects become significant. In addition, the analysis detailed in this work was focused on situations for which quasistatic loading at low strain rates is expected. Another possible window

Table 2

Material properties obtained using the developed framework for the various aging times considered in [35] for an SBR sample thermally aged under 90 °C.

Aging time t_a (days)	Material properties					
	Rubber modulus μ (MPa) Eq. (4)	Number of Kuhn monomers N Eq. (4)	Critical energy release rate G_c (N/mm) Eq. (7)	length scale l_c (mm) Eq. (15)		
14	0.944	68.1	21.5	0.112		
21	1.06	58.7	19.9	0.143		
28	1.16	52.3	18.8	0.17		
60	1.50	48.6	16.2	0.261		

Table 3

Material properties obtained using the developed framework for the various aging times considered in [35] for an SBR sample thermally aged under 100 °C.

Aging time t_a (days)	Material properties					
	Rubber modulus μ (MPa) Eq. (4)	Number of Kuhn monomers <i>N</i> Eq. (4)	Critical energy release rate G_c (N/mm) Eq. (7)	length scale l_c (mm) Eq. (15)		
14	1.21	50.7	18.5	0.179		
21	1.45	40.7	16.6	0.244		
28	1.64	35.3	15.5	0.293		
35	1.84	31	14.5	0.345		
45	2.06	27.4	13.6	0.402		
60	2.95	18.5	11.2	0.640		

for future development is to consider the diffusion of chemical species such as oxygen inside the material and connect chemical gradients to the spatial variation of the material properties. Moreover, revisiting fracture nucleation in such highly aged materials when loaded under complex deformation states, especially for cases where test specimens are smooth (i.e., with no pre-existing cracks), is a topic of ongoing work.

Declaration of competing interest

The authors declare that they have no known competing financial interests or personal relationships that could have appeared to influence the work reported in this paper.

Data availability

The data is cited and publicly available.

Acknowledgments

The authors gratefully acknowledge the support from the National Science Foundation, USA under the award number CMMI-1914565, and the Air-Force Office of Scientific Research (AFOSR) Young Investigator Program (YIP) award #FA9550-20-1-0281. The authors also acknowledge Advanced Research Computing at Virginia Tech for providing computational resources and technical support that have contributed to the results reported within this paper. URL: https://arc.vt.edu/

Appendix A. Finite element discretization

In this section, the FE discretization of the coupled solid-mechanics phase-field problem is described. We begin by establishing the weak-forms associated with coupled displacement-damage problem. Then the finite-element discretization and piecewise approximation corresponding to the displacement and damage fields are established and the resulting discrete equations are provided.

A.1. Weak forms

In accordance with standard practice, by considering an arbitrary vector field $\mathbf{w_u}$ whose components vanish at the corresponding essential boundary segments, the weak form corresponding to the displacement field can be written as follows:

$$\int_{\Omega_0} \mathbf{w_u} \cdot \bar{\mathbf{b}} dV + \int_{\Omega_0} \bar{\mathbf{F}}_u : \mathbf{P} dV = \int_{\Gamma_{0t}} \mathbf{w_u} \cdot \bar{\mathbf{t}} dA \qquad \forall \mathbf{w_u} \text{ with } \mathbf{w_u} = \mathbf{0} \text{ on } \Gamma_{0u}$$
(16)

where we define $\bar{\mathbf{F}}_u = \frac{\partial \mathbf{w_u}}{\partial X}$, i.e., the partial derivative of the arbitrary vector field $\mathbf{w_u}$ with respect to the reference coordinates X.

Equivalently, by considering an arbitrary vector field $\mathbf{w_d}$ whose components vanish at the corresponding essential boundary segments, the weak form corresponding to the damage field can be expressed as

$$\int_{\Omega_{0}} \mathbf{w_{d}} \cdot \left[\frac{G_{c} \alpha'_{(d)}}{c_{\alpha} l_{c}} + \omega'_{(d)} \psi_{0(\mathbf{C})} \right] d\mathbf{V} + \int_{\Omega_{0}} \bar{\mathbf{F}}_{d} \cdot \frac{2G_{c} l_{c}}{c_{\alpha}} \nabla_{\mathbf{X}} dd\mathbf{V}$$

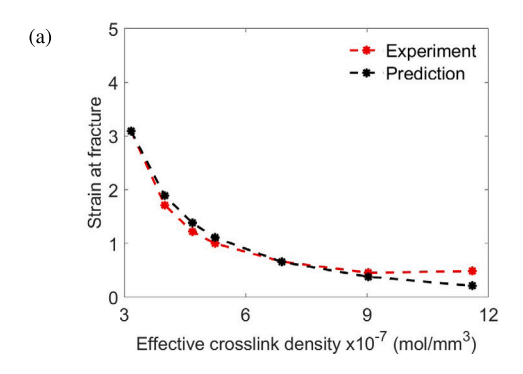
$$\forall \mathbf{w_{d}} \text{ with } \mathbf{w_{d}} = \mathbf{0} \text{ on } \partial B_{d} \tag{17}$$

where similarly $\bar{\mathbf{F}}_d = \frac{\partial \mathbf{w_d}}{\partial \mathbf{X}}$, i.e., the partial derivative of the arbitrary vector field $\mathbf{w_d}$ with respect to the reference coordinates X.

A.2. Finite element discretization

The weak forms (16) and (17) are usually discretized using multifield finite elements. Without loss of generality, in what follows, we consider the case of 2-D problems, with the assumption that the three-dimensional (3D) formulation extends in a straightforward manner. For such problems, the 2-D domain Ω_o is discretized into subdomains called elements and each element consists of nodes. For 2-D problems, the standard and most commonly employed element shapes, i.e., the three-node triangular element and the four-node quadrilateral element are used. For the coupled displacement-phase-field problem in hand, each element node has three nodal degrees of freedom: two for the displacement field and one for the damage field.

The displacement field $\mathbf{u}(\mathbf{X})$ and damage field $d(\mathbf{X})$ are approximated using the nodal displacement and damage vectors, u_i and d_j through their corresponding shape functions, where $i \in [1, \mathsf{ndof}_u]$ and $j \in [1, \mathsf{ndof}_u]$ wherein ndof_u and ndof_d denote the number of degrees of freedom associated with the displacement and damage fields,



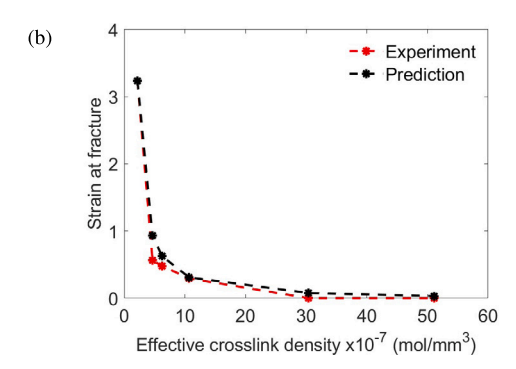


Fig. 10. (a) Strain at failure predictions for two other distinct elastomers as a function of crosslink density. The elastomers have been studied in [10] wherein aging was performed for several aging times at a temperature of 100 °C: (a) a filled SBR material, and (b) a filled NR material.

respectively. The shape functions are established as functions of the Lagrangian coordinates $\{X\}$. Moreover, the displacement field and damage field are considered to be interpolated using the same shape functions, i.e., $N_{u_k}(\mathbf{X}) = N_{d_k}(\mathbf{X}) = N_k(\mathbf{X})$. As such, the displacement and damage fields can be written as follows

$$\mathbf{u}(\mathbf{X}) = \sum_{k=0}^{nnode} \mathbf{N}_{k}(\mathbf{X})\mathbf{u}_{k} = \mathbf{N}_{\mathbf{u}}\bar{\mathbf{u}} \quad \text{and} \quad \mathbf{d}(\mathbf{X}) = \sum_{k=0}^{nnode} \mathbf{N}_{k}(\mathbf{X})\mathbf{d}_{k} = \mathbf{N}_{\mathbf{d}}\bar{\mathbf{d}}$$
(18)

where nnode is the number of nodes in the element, $\mathbf{N_u} = [\mathbf{N_1}, \dots, \mathbf{N_k}, \dots \mathbf{N_{nnode}}]$ where $\mathbf{N_k}(\mathbf{X}) = \begin{bmatrix} N_k & 0 \\ 0 & N_k \end{bmatrix}$, $\mathbf{N_d} = [N_1, \dots, N_k, \dots, N_{nnode}]$, $\bar{\mathbf{u}} = [\mathbf{u_1}, \dots, \mathbf{u_k}, \dots \mathbf{u_{nnode}}]^T$ where $\mathbf{u_k} = \{u_i\}_k$, and $\bar{\mathbf{d}} = [\mathbf{d_1}, \dots, \mathbf{d_k}, \dots \mathbf{d_{nnode}}]^T$ where $\mathbf{d_k} = \{d_j\}_k$. Similarly, we use the same shape functions to approximate the arbitrary vector fields $\mathbf{w_u}$ and $\mathbf{w_d}$ and write:

$$w_u(X) = \sum_k^{\textit{nnode}} N_k(X) w_{uk} = N_u \bar{w}_u \quad \text{and} \quad w_d(X) = \sum_k^{\textit{nnode}} N_k(X) w_{dk} = N_d \bar{w}_d \tag{19}$$

The resulting gradients of the displacement field (i.e., strain field) and the gradient of the phase-field in the reference configuration can be expressed as follows

$$\nabla \mathbf{u}(\mathbf{X}) = \sum_{k}^{nnode} \mathbf{B}_{k}(\mathbf{X}) \mathbf{u}_{k} = \mathbf{B}_{\mathbf{u}} \bar{\mathbf{u}} \quad \text{and} \quad \nabla \mathbf{d}(\mathbf{X}) = \sum_{k}^{nnode} \mathbf{B}_{k}(\mathbf{X}) \mathbf{d}_{k} = \mathbf{B}_{\mathbf{d}} \bar{\mathbf{d}}$$
(20)

where $B_u=[B_{u_1},\dots,B_{u_k},\dots,B_{u_{nnode}}]$ is the standard displacement–strain matrix and $B_d=[B_{d_1},\dots,B_{d_k},\dots,B_{d_{nnode}}]$ is the damage-gradient operator with

$$\mathbf{B}_{\mathbf{u}_{\mathbf{k}}}(\mathbf{X}) = \begin{bmatrix} \partial_{X_{1}} N_{k} & 0 \\ 0 & \partial_{X_{2}} N_{k} \\ \partial_{X_{2}} N_{k} & \partial_{X_{1}} N_{k} \end{bmatrix} \qquad \mathbf{B}_{\mathbf{d}_{\mathbf{k}}}(\mathbf{X}) = \begin{bmatrix} \partial_{X_{1}} N_{k} \\ \partial_{X_{2}} N_{k} \end{bmatrix}$$
(21)

With the above finite element discretization, the weak forms, i.e., Eqs. (16) and (17), become

$$\begin{split} \int_{\Omega_0^e} \mathbf{N}_{\mathbf{u}}^{\mathbf{T}} \bar{\mathbf{b}} \mathrm{d} V - \int_{\Omega_0^e} \mathbf{B}_{\mathbf{u}}^{\mathbf{T}} \mathbf{P} \mathrm{d} V &= -\int_{\Gamma_{0_u}^e} \mathbf{N}_{\mathbf{u}}^{\mathbf{T}} \bar{\mathbf{t}} \mathrm{d} A \\ \int_{\Omega_0^e} \mathbf{B}_{\mathbf{d}}^{\mathbf{T}} \mathbf{H} \mathrm{d} V + \int_{\Omega_0^e} \mathbf{N}_{\mathbf{d}}^{\mathbf{T}} \mathbf{Q} \mathrm{d} V &= 0 \end{split} \tag{22}$$

where
$$\mathbf{H} = \frac{2G_c l_c}{c_a} \nabla_{\mathbf{X}} d$$
 and $\mathbf{Q} = \omega'_{(d)} \psi + \frac{G_c}{c_a l_c} \alpha'_{(d)}$.

This system of coupled equations is solved iteratively using an appropriate numerical procedure by the defining the following element-level residuals for the displacement and phase-field

$$\mathbf{R_{u}^{e}} = \int_{\Omega_{0}^{e}} \mathbf{N_{u}^{T} \bar{b}} dV - \int_{\Omega_{0}^{e}} \mathbf{B_{u}^{T} P} dV + \int_{\Gamma_{0u}^{e}} \mathbf{N_{u}^{T} t_{0}} dA$$

$$\mathbf{R_{d}^{e}} = -\int_{\Omega_{0}^{e}} \mathbf{B_{d}^{T} H} dV - \int_{\Omega_{0}^{e}} \mathbf{N_{d}^{T} Q} dV$$
(23)

and using the corresponding tangents

$$\mathbf{K}_{uu}^{e} = -\frac{\partial \mathbf{R}_{u}^{e}}{\partial \mathbf{u}} , \ \mathbf{K}_{dd}^{e} = -\frac{\partial \mathbf{R}_{d}^{e}}{\partial \mathbf{d}}$$
 (24)

In this work, the staggered scheme of Miehe et al. [62,73] is used and the following system is solved iteratively using a Newton Raphson algorithm

$$\begin{bmatrix} \mathbf{K}_{\mathbf{u}\mathbf{u}}^{\mathbf{e}} & 0 \\ 0 & \mathbf{K}_{\mathbf{d}\mathbf{d}}^{\mathbf{e}} \end{bmatrix}_{n} \begin{bmatrix} \mathbf{u} \\ d \end{bmatrix}_{n+1} = - \begin{bmatrix} \mathbf{R}_{\mathbf{u}}^{\mathbf{e}} \\ \mathbf{R}_{\mathbf{d}}^{\mathbf{e}} \end{bmatrix}_{n}$$
(25)

where the subscript n refers to the converged step and n+1 denotes the next unknown step.

Note that the irreversibility condition $\dot{d} \geq 0$ was enforced through the approach proposed by Wu and Huang [75]. Specifically, a modification to the energy history calculation was introduced as $\mathcal{H}(\mathbf{x},t) = \max_{s \in [0,t]}(\hat{\psi}_0, \psi_0(\mathbf{x}.\mathbf{s}))$ to represent the maximum value of the strain energy density ever reached, where $\hat{\psi}_0$ is a strain energy given by $\frac{3G_c}{16l_c}$ [76]. The term \mathbf{Q} in Eq. (22) is therefore redefined as $\mathbf{Q} = \omega'_{(d)}\mathcal{H} + \frac{G_c}{c_al_c}\alpha'_{(d)}$. This approach suppresses the negative damage values and ensures that the history variable approach is capable of obtaining the correct homogeneous solution. Other numerical treatments could be incorporated as well, such as the approach detailed in the work of Molnár et al. [77], who used a Lagrange Multiplier to enforce a positive damage increment. This approach, however, is computationally expensive, and as such, was not pursued.

Appendix B. Supplementary material

The materials properties for aging temperatures of 90 °C and 100 °C by plugging in the material properties presented in Table 1 into Eqs. (4), (7), and (15) are presented in Table 2, and Table 3, respectively.

Appendix C. Further validation examples

The developed framework in this paper was also validated versus another set of experimental works conducted by Hamed and Zhao [10]. Hamed and Zhao [10] reported the evolution of crosslink density and tensile tests for filled and unfilled sulfur-vulcanized SBR and NR.

The filled materials included 50 phr of N330 carbon black. The SBR specimens contained an antioxidant, while the NR specimens contained 1 phr of dioctylated diphenylamine. The specimens were subjected to air-oven aging at 100 °C for various aging times. All specimens were prepared with an average thickness below the critical thickness to ensure uniform oxidation (thicknesses varied between 0.15 and 0.2 mm). The specimens were subsequently tested in tensile mode under a strain rate of approximately 0.017 s $^{-1}$. The crosslink densities for the unfilled materials were calculated using the classic Flory–Rehner equation, whereas, for the filled samples, the Kraus modification was employed.

Fig. 10 illustrates the evolution of the strain at failure for 50 phr carbon-black filled SBR and NR. As can be seen, we achieve remarkable accuracy in terms of the strain at failure prediction, further demonstrating the robustness of the proposed constitutive framework.

Appendix D. Supplementary data

Supplementary material related to this article can be found online at https://doi.org/10.1016/j.ijmecsci.2023.108721.

References

- Blum GW, Shelton JR, Winn H. Rubber oxidation and aging studies safe limits of sample thickness. Rubber Chem Technol 1951;24(4):999–1016.
- [2] Gillen KT, Wise J, Clough R. General solution for the basic autoxidation scheme. Polym Degrad Stab 1995;47(1):149–61.
- [3] Shaw JA, Jones AS, Wineman AS. Chemorheological response of elastomers at elevated temperatures: Experiments and simulations. J Mech Phys Solids 2005;53(12):2758–93.
- [4] Colin X, Audouin L, Verdu J. Kinetic modelling of the thermal oxidation of polyisoprene elastomers. Part 1: Unvulcanized unstabilized polyisoprene. Polym Degrad Stab 2007;92(5):886–97.
- [5] Wineman A. On the mechanics of elastomers undergoing scission and cross-linking. Int J Adv Eng Sci Appl Math 2009;1(2):123–31.
- [6] Petrikova I, Marvalova B, Nhan P. Influence of thermal ageing on mechanical properties of styrene-butadiene rubber. Const Model Rubber VII 2011;77.
- [7] Spreckels J, Weltin U, Flamm M, Steinweger T, Brüger T. Investigations regarding environmental effects on fatigue life of natural rubber. Const Model Rubber VII 2012;369–74.
- [8] Lion A, Johlitz M. On the representation of chemical ageing of rubber in continuum mechanics. Int J Solids Struct 2012;49(10):1227–40.
- [9] Celina MC. Review of polymer oxidation and its relationship with materials performance and lifetime prediction. Polym Degrad Stab 2013;98(12):2419–29.
- [10] Hamed G, Zhao J. Tensile behavior after oxidative aging of gum and black-filled vulcanizates of SBR and NR. Rubber Chem Technol 1999;72(4):721–30.
- [11] Johlitz M, Diercks N, Lion A. Thermo-oxidative ageing of elastomers: A modelling approach based on a finite strain theory. Int J Plast 2014;63:138–51.
- [12] Wise J, Gillen K, Clough R. An ultrasensitive technique for testing the Arrhenius extrapolation assumption for thermally aged elastomers. Polym Degrad Stab 1995;49(3):403–18.
- [13] Wise J, Gillen K, Clough R. Quantitative model for the time development of diffusion-limited oxidation profiles. Polymer 1997;38(8):1929–44.
- [14] Celina M, Wise J, Ottesen D, Gillen K, Clough R. Correlation of chemical and mechanical property changes during oxidative degradation of neoprene. Polym Degrad Stab 2000;68(2):171–84.
- [15] Achenbach M, Duarte J. A finite element methodology to predict age-related mechanical properties and performance changes in rubber components. Const Model Rubber 2003;59–70.
- [16] Pochiraju K, Tandon G. Modeling thermo-oxidative layer growth in hightemperature resins. J Eng Mater Technol 2006;128(1):107–16.
- [17] Gigliotti M, Grandidier J, Lafarie-Frenot M. Assessment of chemo-mechanical couplings in polymer matrix materials exposed to thermo-oxidative environments at high temperatures and under tensile loadings. Mech Mater 2011;43(8):431–43.
- [18] Steinke L, Veltin U, Flamm M, Lion A, Celina M. Numerical analysis of the heterogeneous ageing of rubber products. Const Model Rubber VII 2011;7:155–60.
- [19] Johlitz M, Retka J, Lion A. Chemical ageing of elastomers: experiments and modelling. Const Model Rubber VII 2011;7:113–8.
- [20] Johlitz M, Lion A. Chemo-thermomechanical ageing of elastomers based on multiphase continuum mechanics. Contin Mech Thermodyn 2013;25(5):605–24.
- [21] Mohammadi H, Bahrololoumi A, Chen Y, Dargazany R. A micro-mechanical model for constitutive behavior of elastomers during thermo-oxidative aging. In: Constitutive models for rubber XI. CRC Press; 2019, p. 542–7.

- [22] Konica S, Sain T. A thermodynamically consistent chemo-mechanically coupled large deformation model for polymer oxidation. J Mech Phys Solids 2020:137:103858.
- [23] Bahrololoumi A, Mohammadi H, Moravati V, Dargazany R. A physically-based model for thermo-oxidative and hydrolytic aging of elastomers. Int J Mech Sci 2021:194:106193.
- [24] Mohammadi H, Morovati V, Korayem A-E, Poshtan E, Dargazany R. Constitutive modeling of elastomers during photo-and thermo-oxidative aging. Polym Degrad Stab 2021:191:109663.
- [25] Shakiba M, Najmeddine A. Physics-based constitutive equation for thermochemically aged elastomers based on crosslink density evolution. J Mech Mater Struct 2022;17(3):229–46.
- [26] Najmeddine A, Xu Z, Liu G, Croft ZL, Liu G, Esker AR, et al. Physics and chemistry-based constitutive modeling of photo-oxidative aging in semi-crystalline polymers. Int J Solids Struct 2022;239–240:111427.
- [27] Ghaderi A, Morovati V, Chen Y, Dargazany R. A physics-informed multi-agents model to predict thermo-oxidative/hydrolytic aging of elastomers. Int J Mech Sci 2022;223:107236.
- [28] Dal H, Kaliske M. A micro-continuum-mechanical material model for failure of rubber-like materials: Application to ageing-induced fracturing. J Mech Phys Solids 2009;57(8):1340–56.
- [29] Volokh K. Hyperelasticity with softening for modeling materials failure. J Mech Phys Solids 2007;55(10):2237–64.
- [30] Volokh K. On modeling failure of rubber-like materials. Mech Res Commun 2010;37(8):684–9.
- [31] Naït-Abdelaziz M, Zaïri F, Qu Z, Hamdi A, Hocine NA. J integral as a fracture criterion of rubber-like materials using the intrinsic defect concept. Mech Mater 2012;53:80–90.
- [32] Hassine MB, Naït-Abdelaziz M, Zaïri F, Colin X, Tourcher C, Marque G. Time to failure prediction in rubber components subjected to thermal ageing: A combined approach based upon the intrinsic defect concept and the fracture mechanics. Mech Mater 2014;79:15–24.
- [33] Sadeg L, Naït-Abdelaziz M, Zaïri F, Ben Hassine M, Ismail J, Qu Z, et al. A large-strain intrinsic default-based fracture criterion for polymers: assessment in biaxial loading and application to ageing. Fatigue Fract Eng Mater Struct 2017;40(8):1201–13.
- [34] Abdelaziz MN, Ayoub G, Colin X, Benhassine M, Mouwakeh M. New developments in fracture of rubbers: Predictive tools and influence of thermal aging. Int J Solids Struct 2019;165:127–36.
- [35] Rezig N, Bellahcene T, Aberkane M, Abdelaziz MN. Thermo-oxidative ageing of a SBR rubber: effects on mechanical and chemical properties. J Polym Res 2020;27(11):1–13.
- [36] Kadri R, Abdelaziz MN, Fayolle B, Hassine MB, Witz J-F. A unified mechanical based approach to fracture properties estimates of rubbers subjected to aging. Int J Solids Struct 2022;234:111305.
- [37] Francfort GA, Marigo J-J. Revisiting brittle fracture as an energy minimization problem. J Mech Phys Solids 1998;46(8):1319–42.
- [38] Li P, Yvonnet J, Combescure C. An extension of the phase field method to model interactions between interfacial damage and brittle fracture in elastoplastic composites. Int J Mech Sci 2020;179:105633.
- [39] Yue Q, Wang Q, Zhou W, Rabczuk T, Zhuang X, Liu B, et al. An efficient adaptive length scale insensitive phase-field model for three-dimensional fracture of solids using trilinear multi-node elements. Int J Mech Sci 2023;253:108351.
- [40] Liu S, Wang Y, Wu W. A modified phase-field model for cohesive interface failure in quasi-brittle solids. Int J Mech Sci 2023;252:108368.
- [41] Liu Y, Feng Y, Wu D, Chen X, Gao W. Virtual modelling integrated phase field method for dynamic fracture analysis. Int J Mech Sci 2023;252:108372.
- [42] Miehe C, Schänzel L-M. Phase field modeling of fracture in rubbery polymers. Part I: Finite elasticity coupled with brittle failure. J Mech Phys Solids 2014;65:93–113.
- [43] Talamini B, Mao Y, Anand L. Progressive damage and rupture in polymers. J Mech Phys Solids 2018;111:434–57.
- [44] Mao Y, Anand L. Fracture of Elastomeric Materials by Crosslink Failure. J Appl Mech 2018;85(8).
- [45] Li B, Bouklas N. A variational phase-field model for brittle fracture in polydisperse elastomer networks. Int J Solids Struct 2020;182–183:193–204.
- [46] Tian F, Zhang M, Zeng J, Li B, Li L. Adaptive stabilized mixed formulation for phase field fracture modeling of nearly incompressible finite elasticity. Int J Mech Sci 2022;236:107753.
- [47] Kumar A, Francfort G, Lopez-Pamies O. Fracture and healing of elastomers: A phase-transition theory and numerical implementation. J Mech Phys Solids 2018;112:523–51.
- [48] Kumar A, Ravi-Chandar K, Lopez-Pamies O. The configurational-forces view of the nucleation and propagation of fracture and healing in elastomers as a phase transition. Int J Fract 2018;213(1):1–16.
- [49] Miehe C, Schänzel L-M, Ulmer H. Phase field modeling of fracture in multiphysics problems. Part I. Balance of crack surface and failure criteria for brittle crack propagation in thermo-elastic solids. Comput Methods Appl Mech Engrg 2015;294:449–85.

ARTICLE IN PRESS

A. Najmeddine and M. Shakiba

International Journal of Mechanical Sciences xxx (xxxx) xxx

- [50] Konica S, Sain T. A reaction-driven evolving network theory coupled with phase-field fracture to model polymer oxidative aging. J Mech Phys Solids 2021;150:104347
- [51] Lake G, Thomas A. The strength of highly elastic materials. Proc R Soc Lond Ser A Math Phys Sci 1967;300(1460):108–19.
- [52] Tanné E, Li T, Bourdin B, Marigo J-J, Maurini C. Crack nucleation in variational phase-field models of brittle fracture. J Mech Phys Solids 2018;110:80–99.
- [53] Marigo J-J, Maurini C, Pham K. An overview of the modelling of fracture by gradient damage models. Meccanica 2016;51(12):3107–28.
- [54] Amor H, Marigo J-J, Maurini C. Regularized formulation of the variational brittle fracture with unilateral contact: Numerical experiments. J Mech Phys Solids 2009;57(8):1209–29.
- [55] Borden MJ, Hughes TJ, Landis CM, Anvari A, Lee IJ. A phase-field formulation for fracture in ductile materials: Finite deformation balance law derivation, plastic degradation, and stress triaxiality effects. Comput Methods Appl Mech Engrg 2016;312:130-66.
- [56] Wise J, Gillen KT, Clough RL. Time development of diffusion-limited oxidation profiles in a radiation environment. Radiat Phys Chem 1997;49(5):565–73.
- [57] Celina M, Wise J, Ottesen D, Gillen K, Clough R. Oxidation profiles of thermally aged nitrile rubber. Polym Degrad Stab 1998;60(2):493–504.
- [58] Celina M, Graham AC, Gillen KT, Assink RA, Minier LM. Thermal degradation studies of a polyurethane propellant binder. Rubber Chem Technol 2000;73(4):678–93.
- [59] Mandal TK, Gupta A, Nguyen VP, Chowdhury R, de Vaucorbeil A. A length scale insensitive phase field model for brittle fracture of hyperelastic solids. Eng Fract Mech 2020:236:107196.
- [60] Bourdin B, Francfort GA, Marigo J-J. Numerical experiments in revisited brittle fracture. J Mech Phys Solids 2000;48(4):797–826.
- [61] Bourdin B, Francfort GA, Marigo J-J. The variational approach to fracture. J Elasticity 2008;91(1):5–148.
- [62] Miehe C, Hofacker M, Welschinger F. A phase field model for rate-independent crack propagation: Robust algorithmic implementation based on operator splits. Comput Methods Appl Mech Engrg 2010;199(45–48):2765–78.

- [63] Ambrosio L, Tortorelli VM. Approximation of functional depending on jumps by elliptic functional via t-convergence. Comm Pure Appl Math 1990;43(8):999–1036.
- [64] Pham K, Amor H, Marigo J-J, Maurini C. Gradient damage models and their use to approximate brittle fracture. Int J Damage Mech 2011;20(4):618–52.
- [65] Arruda EM, Boyce MC. A three-dimensional constitutive model for the large stretch behavior of rubber elastic materials. J. Mech. Phys. Solids 1993;41(2):389–412.
- [66] Song Z, Shen T, Vernerey FJ, Cai S. Force-dependent bond dissociation explains the rate-dependent fracture of vitrimers. Soft Matter 2021;17(27):6669–74.
- [67] Bueche F, Halpin J. Molecular theory for the tensile strength of gum elastomers. J Appl Phys 1964;35(1):36–41.
- [68] Smith TL. Ultimate tensile properties of elastomers. III. dependence of the failure envelope on crosslink density. Rubber Chem Technol 1967;40(2):544–55.
- [69] Mohammadi H, Morovati V, Poshtan E, Dargazany R. Understanding decay functions and their contribution in modeling of thermal-induced aging of cross-linked polymers. Polym Degrad Stab 2020:175:109108.
- [70] Roucou D, Diani J, Brieu M, Colombo D. Experimental identification of fracture toughness of a carbon black-filled styrene butadiene rubber undergoing energy dissipation by Mullins softening. Mech Mater 2020;151:103645.
- [71] Zhi J, Wang Q, Zhang M, Zhou Z, Liu A, Jia Y. Coupled analysis on hyperviscoelastic mechanical behavior and macromolecular network alteration of rubber during thermo-oxidative aging process. Polymer 2019;171:15–24.
- [72] Abaqus AD. Dassault systemes. Providence, RI, USA; 2014.
- [73] Miehe C, Welschinger F, Hofacker M. Thermodynamically consistent phase-field models of fracture: Variational principles and multi-field FE implementations. Internat J Numer Methods Engrg 2010;83(10):1273–311.
- [74] Mandal TK, Nguyen VP, Wu J-Y. Length scale and mesh bias sensitivity of phase-field models for brittle and cohesive fracture. Eng Fract Mech 2019;217:106532.
- [75] Wu J-Y, Huang Y. Comprehensive implementations of phase-field damage models in Abaqus. Theor Appl Fract Mech 2020;106:102440.
- [76] Xing C, Yu T, Sun Y, Wang Y. An adaptive phase-field model with variable-node elements for fracture of hyperelastic materials at large deformations. Eng Fract Mech 2023;281:109115.
- [77] Molnár G, Doitrand A, Jaccon A, Prabel B, Gravouil A. Thermodynamically consistent linear-gradient damage model in Abaqus. Eng Fract Mech 2022;266:108390.